Biochemistry **1998,** *37,* 17965−17976

Ca^{2+}-Dependent Structural Changes in C-type Mannose-Binding Proteins[†,‡]

Kenneth K.-S. Ng, Shaun Park-Snyder, and William I. Weis*

Department of Structural Biology, Stanford University School of Medicine, Stanford, California 94305

Received August 17, 1998; Revised Manuscript Received October 16, 1998

ABSTRACT: C-type animal lectins are a diverse family of proteins which mediate cell-surface carbohydrate-recognition events through a conserved carbohydrate-recognition domain (CRD). Most members of this family possess a carbohydrate-binding activity that depends strictly on the binding of Ca^{2+} at two sites, designated 1 and 2, in the CRD. The structural transitions associated with Ca^{2+} binding in C-type lectins have been investigated by determining high-resolution crystal structures of rat serum mannose-binding protein (MBP) bound to one Ho^{3+} in place of Ca^{2+}, and the apo form of rat liver MBP. The removal of Ca^{2+} does not affect the core structure of the CRD, but dramatic conformational changes occur in the loops. The most significant structural change in the absence of Ca^{2+} is the isomerization of a cis-peptide bond preceding a conserved proline residue in Ca^{2+} site 2. This bond adopts the cis conformation in all Ca^{2+}-bound structures, whereas both cis and trans conformations are observed in the absence of Ca^{2+}. The pattern of structural changes in the three loops that interact with Ca^{2+} is dictated in large part by the conformation of the prolyl peptide bond. The highly conserved nature of Ca^{2+} site 2 suggests that the transitions observed in MBPs are general features of Ca^{2+} binding in C-type lectins.

C-type (Ca^{2+}-dependent) animal lectins are a large family of proteins that bind carbohydrates for many purposes, including recognition of microbial pathogen cell surfaces during innate immune responses, the targeting of leukocytes to sites of inflammation or peripheral lymph nodes, and the endocytosis of serum glycoproteins by the liver. C-type lectins contain a conserved Ca^{2+}-dependent carbohydrate-recognition domain (CRD[1]) of approximately 120 amino acids (*1*). Carbohydrate binding involves the formation of an intimately linked, ternary complex of protein, Ca^{2+}, and carbohydrate. Specifically, two hydroxyl groups of the sugar form direct coordination bonds with a conserved Ca^{2+} and also form hydrogen bonds with amino acids that serve as ligands for this Ca^{2+} (*2*). In addition to its central role in carbohydrate binding, Ca^{2+} has major effects on structural properties such as circular dichroism spectra, intrinsic tryptophan fluorescence, and protease sensitivity (*3*−*10*). The three-dimensional structures of rat serum mannose-binding protein (MBP-A) (*11*), rat liver MBP (MBP-C) (*12*), human MBP (*13*), human E-selectin (*14*), tetranectin (*15*), and galactose-binding (*16*) and selectin-like (*17*) mutants of MBP-A reveal that Ca^{2+} is integral to the structure of three extended loops, designated 1, 3, and 4 (*11*), on the surface of the CRD (Figure 1). MBPs contain two Ca^{2+} sites, designated site 1 and site 2, and sugars interact directly with the Ca^{2+} at site 2 (*2*).

Reversible Ca^{2+} binding is exploited by C-type lectins that function as endocytic receptors. These proteins bind to carbohydrate ligands at the cell surface and are taken up in coated vesicles, which mature into endosomes. Acidification of the endosome causes a loss of Ca^{2+} from the receptors and hence a release of the carbohydrate-bearing ligand, allowing the sorting of the receptor away from its ligand (*18*). Despite the growing wealth of data on the Ca^{2+}-bound structures of C-type lectins, there is little detailed information about structural changes that accompany the removal of Ca^{2+}. The MBPs provide an attractive model system to explore the effects of Ca^{2+} binding on the structure of the C-type CRD, because they are the most thoroughly characterized members of the C-type lectin family. In addition to extensive biochemical (*19*−*24*) and structural (*2, 9, 11, 12, 25, 26*) studies, cassette mutagenesis has been used to identify residues in the MBP-A CRD that influence Ca^{2+}-binding affinity (*27*).

Two distinct MBPs with roughly 50−60% sequence identity are found in the serum (MBP-A) and the liver (MBP-C) of rat, mouse, and macaque (*19, 28, 29*). The MBPs belong to the collectin subclass of C-type lectins, which consist of an NH_2-terminal cysteine-rich domain, a collagen-like domain, an α-helical coiled-coil trimerization domain, and a COOH-terminal C-type CRD (*30*). Structural studies of MBPs have employed fragments containing either the isolated CRD of MBP-A (*2, 9, 11*) or MBP-C (*12*), or the

---

[†] This work is supported by grant GM50565 from the National Institutes of Health. Work at the Stanford Synchrotron Research Laboratory (SSRL) was performed under proposal 3A06. SSRL is operated by the Department of Energy, Office of Basic Energy Sciences. The SSRL Biotechnology Program is supported by the National Institutes of Health, National Center for Research Resources, Biomedical Technology Program, and by the Department of Energy, Office of Biological and Environmental Research.

[‡] Coordinates and structure factors for 1-Ho^{3+}-MBP-A and apo-MBP-C have been deposited in the Protein Data Bank, Brookhaven, NY, with accession codes 1BUU and 1BV4, respectively.

* To whom correspondence should be addressed at Department of Structural Biology, Fairchild Building, Stanford University School of Medicine, Stanford, CA 94305-5126. E-mail: weis@fucose.stanford.edu. Tel: (650) 725 4623. Fax (650) 723 8464.

[1] Abbreviations: CRD, carbohydrate-recognition domain; MBP, mannose-binding protein; MES, 2-(4-morpholino)-ethanesulfonic acid; MPD, 2-methyl-2,4-methylpentanediol; NCS, noncrystallographic symmetry; PEG, poly(ethylene glycol); RMSD, root-mean-square deviation.

10.1021/bi981972a CCC: $15.00

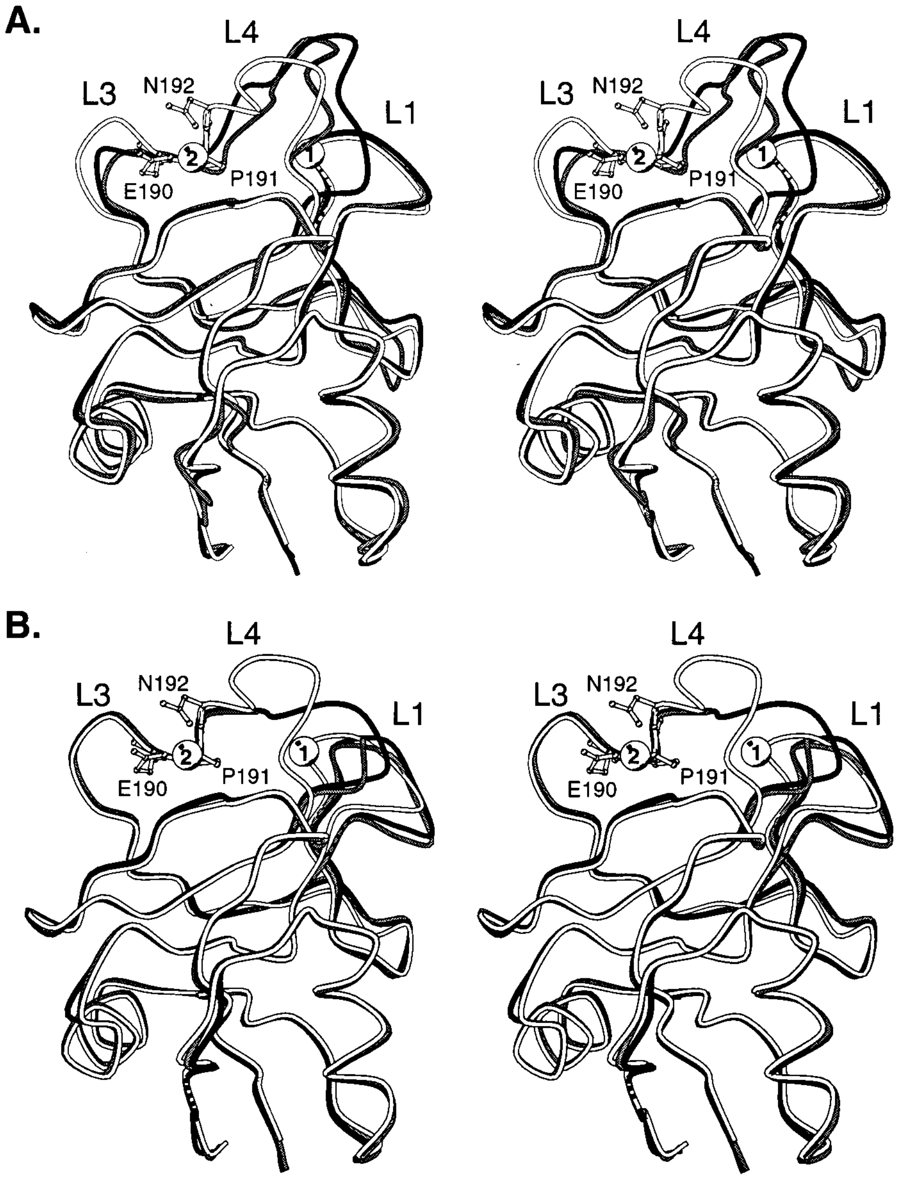

FIGURE 1: Stereoscopic views of superimposed CRDs. (A) The α-carbon traces of one-ion MBP (gray) and copy 1 of apo-MBP (black), each of which contain a *trans*-prolyl peptide bond in Ca^{2+} site 2, have been superimposed onto the α-carbon trace of two-ion MBP (white). Loops 1, 3, and 4 are labeled with an "L". (B) The α-carbon traces of copies 2 (black) and 4 (gray) of apo-MBP, which contain a *cis*-prolyl peptide bond in Ca^{2+} site 2, are superimposed onto the α-carbon trace of two-ion MBP (white). Only the α-carbon atoms from residues 123−165 and 200−220 in MBP-C (which correspond to residues 118−160 and 195−215 of MBP-A) were used in generating the superpositions. Also shown for reference are the positions of the two bound Ca^{2+} (white spheres) and the highly conserved tripeptide sequence motif Glu^{190}-Pro^{191}-Asn^{192} in two-ion MBP. All figures were prepared using BOBSCRIPT (*64*), a modified version of MOLSCRIPT (*65*). Least-squares superpositions were generated in O (*39*).

CRD plus the trimerization domain of MBP-A (*25*) or human MBP (*13*). The isolated CRD of MBP-A or MBP-C forms a dimer in solution and in crystals, whereas the CRD plus the adjacent trimerization region forms trimers. Structures of the CRD in the dimeric and trimeric forms of MBP-A indicate that the structure of the CRD does not change significantly when separated from the adjacent trimerization domain (*25*).

To explore the structural effects of Ca^{2+} binding on C-type animal lectins, we have determined the structures of the CRDs from apo-MBP and a one-ion form of MBP using X-ray crystallography. The structure of the core of the CRD does not change upon the loss of Ca^{2+}, but three loops that participate in Ca^{2+} binding adopt distinct conformations in the absence of Ca^{2+}. A particularly striking conformational change is the Ca^{2+}-dependent isomerization of the peptide bond preceding a highly conserved proline residue at the core of Ca^{2+} site 2.

EXPERIMENTAL PROCEDURES

Materials. Chemicals were from J. T. Baker unless otherwise specified. Poly(ethylene glycol)s (PEG) were from Sigma. $DyCl_3$ and $HoCl_3$ were from Aldrich.

Expression, Purification and Crystallization of One-Ion MBP-A. The clostripain-derived fragment of MBP-A containing the α-helical coiled-coil trimerization domain and the CRD was purified as described previously (*25*). A new construct containing an additional 19 residues NH_2-terminal to the beginning of the clostripain fragment, designated ME-144, was also used. This construct, designed to include the

COOH-terminal portion of the collagenous domain of MBP-A, contains the sequence Ala-Ile-Glu-Val-Ser-Gln-Gly-Pro-Lys-Gly-Gln-Lys-Gly-Asp-Arg-Gly-Asp-Ser-Arg preceding the first residue of the α-helical domain (Ala^{73}).[2] The protein was expressed and purified by affinity chromatography and reverse-phase HPLC as described for other MBP-A constructs (*9*).

The clostripain-derived fragment of MBP-A and ME-144 crystallize isomorphously with one another and in the presence of a variety of lanthanide ions. The one-Dy^{3+} form of the clostripain-digested MBP-A was crystallized by hanging-drop vapor diffusion. HPLC-purified protein (1 μL of 20 mg/mL) was added to 1 μL of well solution (8−12% (w/v) PEG 8000, 100 mM Tris-Cl, pH 8.0, 10 mM NaCl, 0.02% NaN_3, 0.375 mM $DyCl_3$). Crystals appeared over the course of 1−2 weeks. The one-Ho^{3+} form of MBP-A was crystallized using the ME-144 construct in the same way as the clostripain fragment of MBP-A, except that 11−15% (w/v) PEG 3350 and 0.325 mM $HoCl_3$ were used.

Data Collection: *One-Ion MBP-A*. The space group and unit cell dimensions of one-ion MBP-A were determined by precession photography of a capillary-mounted crystal. All data for one-ion MBP were measured using inverse-beam geometry on an R-AXIS-IIc imaging-plate detector (Rigaku), using Cu Kα radiation from a rotating anode (Rigaku; 50 kV, 90 mA, graphite monochromator, 0.3 mm collimator) at a crystal-to-detector distance of 120 mm. Data were integrated with DENZO and scaled with SCALEPACK (*31*). Crystals were flash-cooled to 100 K under a stream of nitrogen gas (Oxford Cryosystems). Data for molecular replacement were measured to maximum Bragg spacings of 2.4 Å from a clostripain fragment MBP-A crystal (size 0.25 × 0.25 × 0.12 mm^3) grown with $DyCl_3$ and adapted stepwise to synthetic mother liquor containing 0%, 5%, 10%, 15%, and 20% glycerol before cooling (96.8% complete; $R_{sym} = 0.044$; Friedel mates treated as separate observations). After obtaining a molecular replacement solution from these data, we measured a new data set to 2.30 Å ($R_{sym} = 0.031$; 91.1% complete; Friedel mates treated as separate observations) from a larger Dy^{3+}-containing crystal (size 0.4 × 0.3 × (0.2−0.1) mm^3) that had been adapted stepwise to synthetic mother liquor containing 5%, 7.5%, 10%, and 15% 2,4-methylpentanediol (MPD). Data used for the final refinement were collected from a ME-144 crystal, size 0.45 × 0.4 × 0.15 mm^3, grown in the presence of $HoCl_3$ and adapted stepwise in mother liquor containing 5%, 10%, and 15% MPD. Statistics from this data set are given in Table 1.

Table 1: Crystallographic Data[a]

	$1\text{-}Ho^{3+}$-MBP-A	apo-MBP-C
space group	$P2_13$	$P2_1$
unit cell parameters[b]	$a = 94.4$ Å	$a = 32.4$ Å, $b = 132.6$ Å, $c = 46.8$ Å, $\beta = 94.3°$
maximum resolution (Å)	1.90	1.85
no. of independent reflections	20 530	33 667
completeness (%)	95.1 (88.0)	99.9 (99.8)
average redundancy	7.0 (3.9)	3.7 (3.5)
% > $3\sigma(I)$	83.2 (52.6)	86.5 (62.4)
R_{sym}[c]	0.056 (0.215)	0.039 (0.260)

[a] All statistics calculated with a low-resolution cutoff of 50 Å. Numbers in parentheses are for the highest-resolution shell: 1.97−1.90 Å for MBP-A and 1.92−1.85 Å for MBP-C. [b] From post-refinement in SCALEPACK (*31*). [c] $R_{sym} = \sum_{\mathbf{h}} \sum_i (|I_i(\mathbf{h}) - \langle I(\mathbf{h})\rangle|/\sum_{\mathbf{h}} \sum_i I_i(\mathbf{h}))$ where $I_i(\mathbf{h})$ is the i^{th} measurement and $\langle I(\mathbf{h})\rangle$ is the weighted mean of all measurements of $I(\mathbf{h})$.

Structure Solution and Refinement of One-Ion MBP-A. The data measured from a Dy^{3+}-substituted crystal cryoprotected with glycerol were used for molecular replacement. The asymmetric unit is too small to contain an entire trimer, indicating that the molecular and crystallographic 3-fold axes are coincident. The calculated solvent content of the crystal is 69% for one protomer in the asymmetric unit and 38% for two protomers in the asymmetric unit. Self-rotation functions and native Patterson syntheses did not show any significant peaks, suggesting that the asymmetric unit contains a single protomer. A protomer (helix + CRD) from the Ca^{2+}-bound trimer structure (*25*), which at the time of these calculations was only partially refined ($R = 0.256$ to 2.5 Å), was used as a search model. No Ca^{2+} or water molecules were present in the search model, but individual temperature factors were retained. X-PLOR (v. 3.54) (*32*) was used for all molecular replacement calculations. A cross-rotation function was computed with data between 10 and 4 Å and a maximum Patterson vector length of 45 Å. No single solution stood out, but Patterson correlation refinement (*33*) produced a clear solution (correlation coefficient 0.034, next highest 0.031) from the third-highest cross-rotation function peak. A translation search of this rotation solution gave an unambiguous answer (18.7σ over the mean; next highest 6.9σ). Rigid body refinement of this model, first as a single unit and then treating the helix and CRD as independent rigid bodies, gave an R value of 0.429 for data between 10 and 2.8 Å. A single site obtained from an anomalous difference Patterson corresponds to Ca^{2+} site 1, confirming the molecular replacement solution. Difference Fourier maps ($|F_o| - |F_c|$) computed with the model phases gave a large peak at Ca^{2+} site 1, but no peak at site 2, indicating that only site 1 was occupied by Dy^{3+}.

The molecular replacement model was rigid-body-refined against the data obtained from another Dy^{3+}-containing crystal using MPD as the cryoprotectant, and then subjected to several rounds of minimization and temperature factor refinement to 2.3 Å ($R = 0.250$). Because $\Delta f'' = 9.7e$ for Dy at the Cu Kα wavelength, Friedel mates were treated as separate observations and the corrections for anomalous scattering applied. At this point, a 1.90 Å resolution data set (Table 1) was measured from an isomorphous Ho^{3+}-containing crystal of ME-144, and refinement was completed using these data. The Dy^{3+} was replaced with Ho^{3+} in the partially refined model and rigid-body-refined at 2.8 Å ($R = 0.308$). Unlike Dy, Ho has a small $\Delta f''$ at Cu Kα, so Friedel mates were merged for data processing and refinement, and the imaginary part of the anomalous scattering was ignored. However, $\Delta f' = -12.3e$ for Ho at Cu Kα, so the Ho scattering factor was corrected for this term. A random 10% of the data was used for calculation of R_{free}, but this test set was biased by the earlier rounds of refinement against the Dy^{3+}-containing crystal data. Therefore, the model was subjected to simulated annealing refinement at 4000 K to remove any memory of the previous data from the model. This was followed by several rounds of minimization,

---

[2] Kurt Drickamer, personal communication.

Table 2: Refinement[a]

	1-Ho^{3+}- MBP-A	apo-MBP-C
no. of reflections in working set	18 510	29 637
no. of non-hydrogen atoms	1 325	3 472
no. of water molecules	171	235
R_{cryst}[b]	0.198 (0.233)	0.211 (0.237)
R_{free}[b]	0.214 (0.271)	0.256 (0.308)
model geometry:		
bond length rmsd (Å)	0.005	0.007
bond angle rmsd (deg)	1.3	1.4
Ramachandran plot[c]		
% in most favored regions	93.2	93.3
% in additional allowed regions	6.0	6.7
% in generously allowed regions	0.8	0.0
temperature factors (Å^2)		
averages (protein atoms only)		
copy 1	26.8	27.6
copy 2		26.1
copy 3		35.9
copy 4		21.5
main chain bonded rmsd	1.3	2.4
main chain angle rmsd	2.1	3.4
side chain bonded rmsd	2.1	3.7
side chain angle rmsd	3.2	5.2

[a] Numbers in parentheses are for highest-resolution shell: 1.97−1.90 Å for MBP-A, 1.92−1.85 Å for MBP-C. [b] R_{cryst} and R_{free} = $\Sigma_{\mathbf{h}} ||F(\mathbf{h})_{obs}| - |F(\mathbf{h})_{calc}||/\Sigma_{\mathbf{h}} |F(\mathbf{h})_{obs}|$ for reflections in the working and test sets (*61*), respectively. [c] As defined in PROCHECK (*62*).

temperature factor refinement, and manual model adjustment, ultimately using data between 10 and 1.90 Å, with no bulk solvent correction. Final rounds of refinement were performed with the programs CNS (*34*), using all data with $|F| > 0$ between 50 and 1.90 Å, a maximum-likelihood amplitude target (*35*), and a dual-scale bulk solvent correction (*36*). Electron density is weak for the first four residues of the helical domain (residues 73−76), and no electron density is visible for the collagen-like portion of ME-144 preceding the first residue of the helical domain, suggesting that this portion is linked flexibly to the protein. This observation is consistent with the protease sensitivity of this site, since other arginine residues in the protein are not cut by clostripain (*25*). The final model consists of residues 73−221 of MBP-A, one Ho^{3+}, and 171 water molecules. The refinement and model geometry are summarized in Tables 1 and 2.

Expression, Purification and Crystallization of apo-MBP-C. The subtilisin fragment of MBP-C containing the entire CRD was expressed and purified as described previously (*12*). The apo form of MBP-C was crystallized by hanging-drop vapor diffusion. HPLC-purified protein (1 μL of 12 mg/mL) which had been neutralized to pH 7.5 with 15 mM NaOH was added to 1 μL of well solution (8−12% PEG (w/v) PEG 8000, 100 mM Na-MES, pH 6.1, 200 mM LiCl, 2 mM EDTA, 0.02% NaN_3). Crystals were observed over the pH range 6.0−7.0, but pH 6.1−6.2 appeared to be optimal. Clusters of crystals appeared over the course of a few days and reached full size in about a month. Crystals dissected from clusters were used to seed fresh hanging drops in which the concentration of protein was reduced to 5 mg/mL. For data collection, crystals grown from the macroseeded drops were harvested into a stabilization buffer consisting of well solution in which the amount of PEG 8000 had been increased to 14% (w/v). The crystals appear to be stable even when the pH of the stabilization buffer is reduced to 5.0, although diffraction was never measured from crystals exposed to this pH.

Data Collection: *apo-MBP-C***.** The space group and unit cell dimensions of the apo-MBP-C crystal were determined by precession photography of a capillary-mounted crystal. The first set of data for apo-MBP-C was measured from crystals (roughly 0.2 × 0.2 × 0.1 mm^3) adapted stepwise to solutions containing stabilization buffer plus glycerol (final concentration 25%) prior to flash-cooling to 100 K. These data were measured on a R-AXIS IIc detector using Cu Kα radiation from a rotating anode, at a crystal-to-detector distance of 130 mm, and processed with DENZO and SCALEPACK (40−2.2 Å; $R_{sym} = 0.05$). The data used for the final rounds of refinement and map calculation were measured from a crystal adapted to solutions containing the stabilization buffer plus PEG 400 (final concentration 25%). Data were measured from a Mar 300 mm detector (Mar-Research) using 1.08 Å wavelength radiation at the Stanford Synchrotron Research Laboratory beamline 7−1. Data were recorded as 118 1.5° oscillations, at a crystal-to-detector distance of 220 mm. Data were processed with DENZO and SCALEPACK (*31*). Each data set was put on a quasi-absolute scale using TRUNCATE (*37*). Data processing statistics are presented in Table 1.

Structure Solution and Refinement of apo-MBP-C. The data measured on the rotating anode were used for molecular replacement calculations. The solvent content of the apo-MBP-C crystal was calculated to be 68% and 36% if either one or two dimers were present in the asymmetric unit. A self-rotation function showed one significant peak and several smaller peaks corresponding to 2-fold rotation axes, but no significant peaks corresponding to 3-fold or 4-fold rotation axes (not shown). The search model for molecular replacement calculations consisted of the Ca^{2+}-bound CRD dimer from the refined structure of Ca^{2+}-bound MBP-C (*12*) in which residues 165−200 were omitted, because it was suspected that these residues might differ in the absence of Ca^{2+}. The refined individual temperature factors were retained. Cross-rotation functions calculated using data between 10 and 4 Å Bragg spacings, and a maximum Patterson vector length of 40 Å, gave two solutions (6.2σ above the mean; next highest solution 4.0σ). Patterson-correlation refinement (*33*) of each rotation function yielded correlation coefficients of 0.13 (next highest 0.09). Each rotation function solution was used to calculate a translation function using data from 10 to 4 Å, yielding a pair of solutions (both at 4.9σ above the mean; next highest solution 4.3σ). The relative positions of the two dimers in the asymmetric unit were determined by fixing one translation function solution and translating the other along the monoclinic *b* axis for each of the four possible origins in the *ac* plane. This procedure yielded one solution (9.9σ above the mean). The positions of each of the four copies in the asymmetric unit were refined as rigid bodies against data between 10 and 4 Å, yielding an *R* value of 0.435. The crystal packing was reasonable, with gaps between molecules at the positions where loops had been deleted from the search model. X-PLOR (v. 3.54) (*32*) was used for all molecular replacement calculations.

Initial rounds of refinement were performed using the rotating anode data. Noncrystallographic symmetry restraints were not imposed at any point during refinement, because test calculations indicated that both the conventional and cross-validated *R* values increased even with weak NCS restraints. Throughout the course of refinement, regions where the model fit the electron density poorly or had poor geometry were omitted and rebuilt according to simulated annealing omit maps (*38*). Electron density maps were initially calculated to a maximum resolution of 2.8 Å using phases from the molecular replacement search model. A model for the loops in three of the four CRDs in the asymmetric unit was constructed by iterative rounds of model building using the program O (*39*) and reciprocal space refinement using the program X-PLOR (*32*) ($R_{cryst} = 0.26$, $R_{free} = 0.32$). The electron density for a large segment of the loops from copy 3 (residues 166−173 and 179−199) was not clear enough to model unambiguously, however. At this point, higher-resolution data were obtained at a synchrotron source (Table 1) and used for refinement. Thin shells of data were selected for cross-validation in order to minimize bias from noncrystallographic symmetry. After further rounds of positional refinement, rebuilding, refinement of a bulk solvent model, and addition of solvent molecules (40−1.85 Å, $R_{cryst} = 0.22$, $R_{free} = 0.30$), tests indicated that electron density maps were significantly improved by continuing refinement using a maximum-likelihood target (*35*) and a dual-scale bulk solvent model (*36*), as implemented in the program CNS (*34*). An overall anisotropic temperature factor tensor (*40*) was applied throughout (final values: $B_{11} = -0.86$ Å^2, $B_{22} = 3.66$ Å^2, $B_{33} = -2.81$ Å^2, $B_{13} = -0.39$ Å^2). Prior to the continuation of refinement with the maximum-likelihood target, a new set of reflections were selected for cross-validation, because the shells that had been selected previously did not extend evenly enough over reciprocal space for the reliable calculation of cross-validated σ_A weights. Torsional dynamics simulated annealing refinement starting at 2000 K was performed to reduce bias due to inclusion of reflections from the old working set in the new test set. The improvement in the resulting electron density maps allowed the modeling of the remainder of copy 3, although the fit to the electron density was only acceptable in maps calculated to a high-resolution limit of 3.5 Å. Electron density maps calculated to higher-resolution limits were consistent with the maps calculated with lower-resolution limits, but there were numerous breaks in main chain and side chain density for the loops in copy 3. Therefore, these residues were omitted from the final model. The superior fit of the loops in maps calculated at lower resolution likely reflects the presence of either static or dynamic disorder. Increased disorder upon the loss of Ca^{2+} may be attributed to the loss of stabilizing interactions mediated by Ca^{2+}.

The final model contains four independent copies of the MBP-C CRD, with the following residues omitted: residues 111−114 at the NH_2-termini of all copies; residues 170−171 of copy 2; residues 165−173, 179−199, and 226 of copy 3; and residues 194−197 of copy 4. In addition to the loop regions, the following surface side chains are not well-defined at 1σ contour in the final, refined electron density maps: Arg^{122}, Arg^{123}, Asn^{127}, Arg^{128}, Lys^{130}, Glu^{188}, and Glu^{190} in copy 1; Glu^{147} and Arg^{180} in copy 2; Tyr^{116}, Arg^{122}, Arg^{123}, Lys^{130}, Lys^{157}, Arg^{180}, Arg^{182}, Tyr^{183}, and Asn^{199} in copy 3; and Tyr^{116}, Lys^{157}, Glu^{170}, and Asn^{193} in copy 4. The side chains of Glu^{198} in copy 1, Asn^{127} in copy 2, and Lys^{114} in copy 4 have been modeled in two conformations. Model geometry and temperature factor statistics are summarized in Table 2. Luzzati analysis (*41*) suggests that the coordinate error is approximately 0.25 Å. Copy 4 has a significantly lower overall temperature factor than copies 1 and 2, and copy 3 has the highest overall temperature factors (Table 2). These differences are probably due to differences in the extent of packing within the crystal lattice.

RESULTS

Nomenclature for Different Forms of MBP. In this paper, the 2-Ca^{2+} forms of MBPs A and C, whose three-dimensional structures are very similar (*12*) (Table 3), are designated two-ion MBP. The one-Ho^{3+} form of MBP-A is designated as one-ion MBP, whereas MBP-C which is free of metal ions is designated as apo-MBP. The structure of 1-Ho^{3+} MBP-A contains the entire CRD plus the adjacent trimerization domain, whereas the structures of apo-MBP-C contain only the CRD. The crystals of apo-MBP contain four copies of the CRD in the asymmetric unit, which will be referred to as copies 1−4. The four copies represent independent views of the molecule in distinct lattice environments.

General Features of Metal-Ion-Induced Conformational Changes in MBPs. The Ca^{2+}-binding sites in MBPs are largely formed by loops 1, 3, and 4 (*11*) (Figures 1 and 2). Residues from loops 1 and 4 constitute site 1, whereas site 2 is formed by residues from loops 3 and 4, as well as two amino acids from β-strand 4 (Figure 2A,B). One-ion MBP and apo-MBP show that the loss of Ca^{2+} induces many changes in the loop regions, while leaving the lower two-thirds of the CRD essentially unaffected (Figure 1). Pairwise superpositions between the main chain atoms of the lower portion of the CRD in the four copies of apo-MBP, one-ion MBP, and two-ion MBP yield RMSDs of 0.3−0.6 Å for all main chain atoms, which are similar to RMSDs obtained by comparing noncrystallographically related copies of the Ca^{2+}-bound protein or the Ca^{2+}-bound form of MBP-A with that of MBP-C (Table 3A). In contrast, RMSDs calculated by superimposing entire CRDs or individual loop regions are in the range of 1−2 Å, indicating that substantial conformational changes occur in the loops (Table 3A−C). This is graphically demonstrated by superimposing the lower 60% of the CRD (residues 118−165 and 200−225 in MBP-C) and comparing the paths taken by the α-carbon backbone (Figure 1). In addition to these large changes in the path of the protein backbone, substantial conformational changes in the side chains of residues that serve as Ca^{2+} ligands are also observed (Figure 2).

The apparent structural rigidity of the lower portion of the CRD likely results from the stabilizing interactions provided by secondary structure elements, two disulfide bonds, and a well-packed hydrophobic core (*11*). In contrast, the conformations adopted by the loops which interact with Ca^{2+} change in several different ways, depending in part on the stabilizing interactions provided by neighboring molecules in the crystal lattice. It is likely that the crystal lattice selects major conformations from the ensemble present in solution, although it is possible that crystal lattice packing may select minor solution conformations. As discussed below, however, similar conformations are seen in more than one lattice environment, indicating that the structures observed in the crystals reflect the inherent structural propensities of the protein.

Table 3: RMSDs of Superimposed Coordinates for Two-ion, One-ion, and apo-MBP[a]

A. Global Superpositions[b]

		two-ion				one-ion MBP	apo MBP-C			
		MBP-A		MBP-C						
	copy no.	1	2	1	2		1	2	3	4
two-ion MBP-A	1	−	0.40	0.51	0.58	0.27	0.54	0.55	0.56	0.52
	2	0.34	−	0.65	0.71	0.44	0.63	0.70	0.66	0.66
two-ion MBP-C	1	0.62	0.70	−	0.25	0.52	0.44	0.36	0.42	0.26
	2	0.74	0.82	0.32	−	0.59	0.43	0.35	0.49	0.34
one-ion MBP		1.34	1.42	1.48	1.53	−	0.50	0.52	0.52	0.50
apo MBP	1	1.50	1.56	1.42	1.38	1.08	−	0.30	0.37	0.39
	2	1.57	1.62	1.47	1.44	1.91	1.47	−	0.33	0.25
	3								−	0.31
	4	0.97	1.03	0.84	0.95	1.53	1.20	0.44		−

		two-ion				one-ion MBP	apo MBP-C		
		MBP-A		MBP-C					
	copy no.	1	2	1	2		1	2	4
B. Superpositions of all Loops or Only Loop 1[c]									
two-ion MBP-A	1	−	0.19	0.70	0.84	2.04	2.19	2.37	1.40
	2	0.12	−	0.75	0.88	2.09	2.25	2.39	1.43
two-ion MBP-C	1	0.19	0.17	−	0.37	2.18	2.08	2.25	1.24
	2	0.23	0.20	0.16	−	2.21	2.04	2.15	1.34
one-ion MBP		0.20	0.26	0.28	0.35	−	1.56	2.82	2.25
apo MBP	1	0.31	0.29	0.28	0.28	0.39	−	2.15	1.70
	2	0.91	0.88	0.91	0.91	0.96	0.91	−	0.62
	4	0.41	0.41	0.41	0.44	0.42	0.47	0.91	−
C. Superpositions of Only Loops 3 or 4[d]									
two-ion MBP-A	1	−	0.09	0.25	0.30	2.04	2.24	2.53	1.93
	2	0.15	−	0.22	0.33	2.04	2.25	2.54	1.94
two-ion MBP-C	1	0.25	0.22	−	0.07	2.10	1.67	0.17	0.17
	2	0.30	0.33	0.25	−	2.10	1.70	0.18	0.18
one-ion MBP		2.04	2.04	2.03	1.96	−	1.14	2.11	2.12
apo MBP	1	2.24	2.25	2.20	2.15	1.84	−	2.15	1.74
	2	2.53	2.54	2.51	2.43	2.89	2.47	−	0.04
	4	1.93	1.94	1.94	1.94	2.09	1.33	0.46	−

[a] Only main chain atoms are included in the superpositions. All superpositions were performed using the program LSQMAN (*63*). The "copy no." entry refers to the individual copies in the asymmetric unit of the crystal. The two-ion MBP-A (*2*) and MBP-C (*12*) structures each contain two copies of the CRD in the asymmetric unit of the crystal, and the apo-MBP-C crystal reported here contains 4 copies in the asymmetric unit. [b] Above diagonal: CRD core (residues 123−165 and 200−220 of MBP-C or residues 118−160 and 195−215 of MBP-A; 256 atoms). Below diagonal: entire CRD, except for first β-strand, which differs somewhat between the MBPs A and C (residues 123−220 of MBP-C or 118−225 of MBP-A; 392 atoms). Copy 3 of apo-MBP was left out of the second set of comparisons, because the loop regions are disordered and could not be modeled with confidence. [c] Above diagonal: loops 1−4 (residues 165−199 of MBP-C or 160−194 of MBP-A; 140 atoms). Below diagonal: loop 1 (residues 164−173 of MBP-C or 159−168 of MBP-A; 40 atoms). [d] Above diagonal: loop 3 (residues 185−191 of MBP-C or 180−186 of MBP-A; 28 atoms). Below diagonal: loop 4 (residues 191−200 of MBP-C or 186−195 of MBP-A; 40 atoms).

Changes Associated with the Loss of Metal at Site 2. Biochemical and crystallographic data indicate that Ho^{3+} and other trivalent lanthanide ions mimic the effects of Ca^{2+} both functionally (*9*) and structurally (*11*, *26*), and we assume herein that Ho^{3+} and Ca^{2+} are equivalent. The structure of one-ion MBP provides a view of the protein with a lanthanide ion bound to Ca^{2+} site 1 while Ca^{2+} site 2 is empty. The region of the protein around Ca^{2+} site 1 is essentially unchanged relative to the Ca^{2+}-saturated structures of MBPs reported previously (Figures 2A,B,E and 3A,B) (*2*, *12*, *13*). Previous structures of MBP-A bound to two Ho^{3+} or Yb^{3+} also show that the geometry of lanthanide ion binding is identical to that of Ca^{2+} binding (*11, 26*). The one-ion structure therefore demonstrates that Ca^{2+} site 1 can form independently of Ca^{2+} site 2.

In contrast to site 1, large changes occur in loops 3 and 4 around the vacant Ca^{2+} site 2 (compare Figure 2, parts b and e). These two loops consist of a stretch of 14 amino acids which, when Ca^{2+} is bound at site 2, are pinned down to the rest of the protein by ligation of the Ca^{2+} by Glu^{185} from loop 3, Asn^{187} and Glu^{193} from loop 4, and Asn^{205} and Asp^{206} from β-strand 4 (equivalent to Glu^{190}, Asn^{192}, Glu^{198}, Asn^{210}, and Asp^{211}, respectively, in MBP-C). In one-ion MBP, the absence of Ca^{2+} at site 2 causes the backbone of loops 3 and 4 to move by up to 4 Å, and side chain atoms move by as much as 12 Å (compare Figure 3, parts A and B).

The major determinant of the conformations of loops 3 and 4 is the conformation of the peptide bond preceding Pro^{186} in MBP-A (Pro^{191} in MBP-C) (Figure 2). This proline residue, which defines the junction between loops 3 and 4, is highly conserved among the C-type lectins. The peptide bond preceding this residue adopts the cis conformation when Ca^{2+} site 2 is occupied (Table 4, Figure 4A) (*11*−*15*). The cis-peptide conformation is critical for positioning the flanking residues for Ca^{2+} binding to site 2 (Figure 2A,B). In one-ion MBP, the electron density around Pro^{186} shows that the peptide bond preceding this residue is in the trans

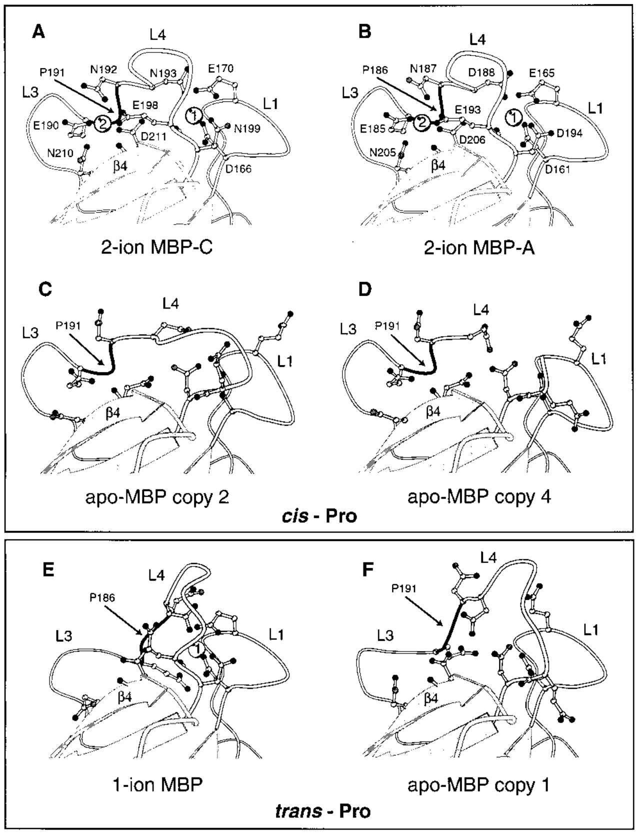

FIGURE 2: Conformational changes upon the loss of Ca^{2+}. *cis*-Pro is present in site 2 of two-ion MBP-C (A) (*12*) or MBP-A (B) (*2*), apo-MBP copy 2 (C), and apo-MBP copy 4 (D). *trans*-Pro is present in one-ion MBP (E) and apo-MBP copy 1 (F). Each CRD is drawn from the same view as the superpositions in Figure 1. The α-carbon backbone trace for loops 1−4 (residues 165−199 of MBP-C and residues 160−194 of MBP-A) is drawn in white. The rest of the CRD is drawn in light gray with arrows representing *β*-strands. All of the residues that serve as Ca^{2+} ligands are drawn as balls and sticks and are labeled in the two-ion forms. Carbon, nitrogen, oxygen, and calcium are shown as white, black, gray, and large white spheres, respectively. The arrow points to the backbone (black) of the conserved proline residue in Ca^{2+} site 2.

Table 4: Conformation of Peptide Bond Preceding Ca^{2+} Site 2 Proline

structure	conformation of proline
two-ion MBP	cis
one-ion MBP	trans
apo-MBP	
copy 1	trans
copy 2	cis
copy 3	*a*
copy 4	cis

[a] Low-resolution electron density is more consistent with the cis conformation. High-resolution electron density is broken and ambiguous around the Glu^{190}-Pro^{191} peptide bond.

conformation (Table 4, Figure 4B). Thus, cis−trans isomerization of Pro^{186} is associated with the large changes observed in loops 3 and 4 in one-ion MBP.

Conformational Changes upon the Loss of Two Ca^{2+} from the MBP CRD. The loss of two Ca^{2+} from the CRD leads to a wider spectrum of conformational changes than those seen in one-ion MBP, where Ca^{2+} is absent only at site 2 (Figures 1 and 2C,D,F). As in the case of one-ion MBP, the structure of the core secondary structure elements is not affected by the loss of Ca^{2+}, and significant changes are restricted to loops 1, 3, and 4.

The absence of Ca^{2+} at site 1 alters the positions of side chains in loop 1 and also changes the disposition of loop 1 relative to the core of the CRD. Loop 1 is well-defined in all of the structures of two-ion and one-ion MBP, as well as copies 1 and 4 of apo-MBP. In apo-MBP, residues 170 and 171 at the tip of the loop in copy 2, and nearly the entire loop in copy 3, are somewhat disordered, even though the structures of these loops are well-defined in electron density maps calculated to a maximum resolution of 3.5 Å. Superimposing the CRD cores of apo-MBP, one-ion MBP, and two-ion MBP shows that the loss of Ca^{2+} from site 1 allows loop 1 to move as a flap, with the tip of the flap moving by 2−3 Å from the position adopted in the presence of Ca^{2+} (Figure 1B). If only residues 165−173 are superimposed onto the corresponding residues of the Ca^{2+}-saturated MBPs (Figure 5), the RMSDs between Ca^{2+}-free and Ca^{2+}-bound forms of the loop are as low as the RMSDs between noncrystallographically related copies of the Ca^{2+}-bound loop (Table 3c), confirming that the torsion angles in the main chain of the loop itself do not change significantly upon the loss of Ca^{2+} from site 1. It is also interesting that one of the highly conserved bidentate ligands for Ca^{2+} site 1 from loop 1, Asp^{166} in MBP-C (Asp^{161} in MBP-A), retains its position despite the loss of Ca^{2+} (Figure 3A,C). This residue is able to form new hydrogen-bond partners in the absence of Ca^{2+} in the three copies (all but copy 3) of apo-MBP in which this residue is well-ordered (Figure 3c), suggesting that it is important for maintaining structural integrity in this region of the protein in the absence of Ca^{2+}. In contrast, a second, less-conserved bidentate ligand, Glu^{170} in MBP-C (Glu^{165} in MBP-A), rotates away from the binding site in the two copies (1 and 4) of apo-MBP in which this residue is well-ordered (Figures 2D,F and 5). In copies 2 and 3, even though the electron density for Glu^{170} and the adjacent portion of the main chain cannot be modeled with confidence, the observed electron density suggests that the position of the side chain is likely to be in a highly exposed conformation.

As observed in one-ion MBP, the most dramatic change affecting the structure of loops 3 and 4 in apo-MBP is in the conformation of the conserved proline in Ca^{2+} site 2 (Pro^{191} in MBP-C; equivalent to Pro^{186} in MBP-A) (Table 4). In copy 1 of apo-MBP, the prolyl peptide bond adopts the trans conformation (Figure 4d), and the structure of loop 3 is more similar to that in one-ion MBP than the same loop in either two-ion MBP or the other copies of apo-MBP (Figure 2E,F and Table 3C). In contrast, copies 2 and 4 of apo-MBP have the prolyl peptide bond in the cis conformation, and loop 3 in these copies has a conformation very similar to that observed in two-ion MBP (Figure 2A−D and Table 3C), even though the interactions that would be mediated by Ca^{2+} at site 2 are missing. The conformation of the prolyl peptide bond thus acts as a switch between two distinct sets of conformations of loop 3. In copy 3 of apo-MBP, the electron density of loop 3 is poorly defined, suggesting that this loop is mobile and possibly alternating between the conformations determined by the cis or trans conformation of Pro^{191}, although electron density maps calculated to a maximum resolution of 3−4 Å suggest that the conformation of the loop is more consistent with the peptide bond adopting the cis conformation.

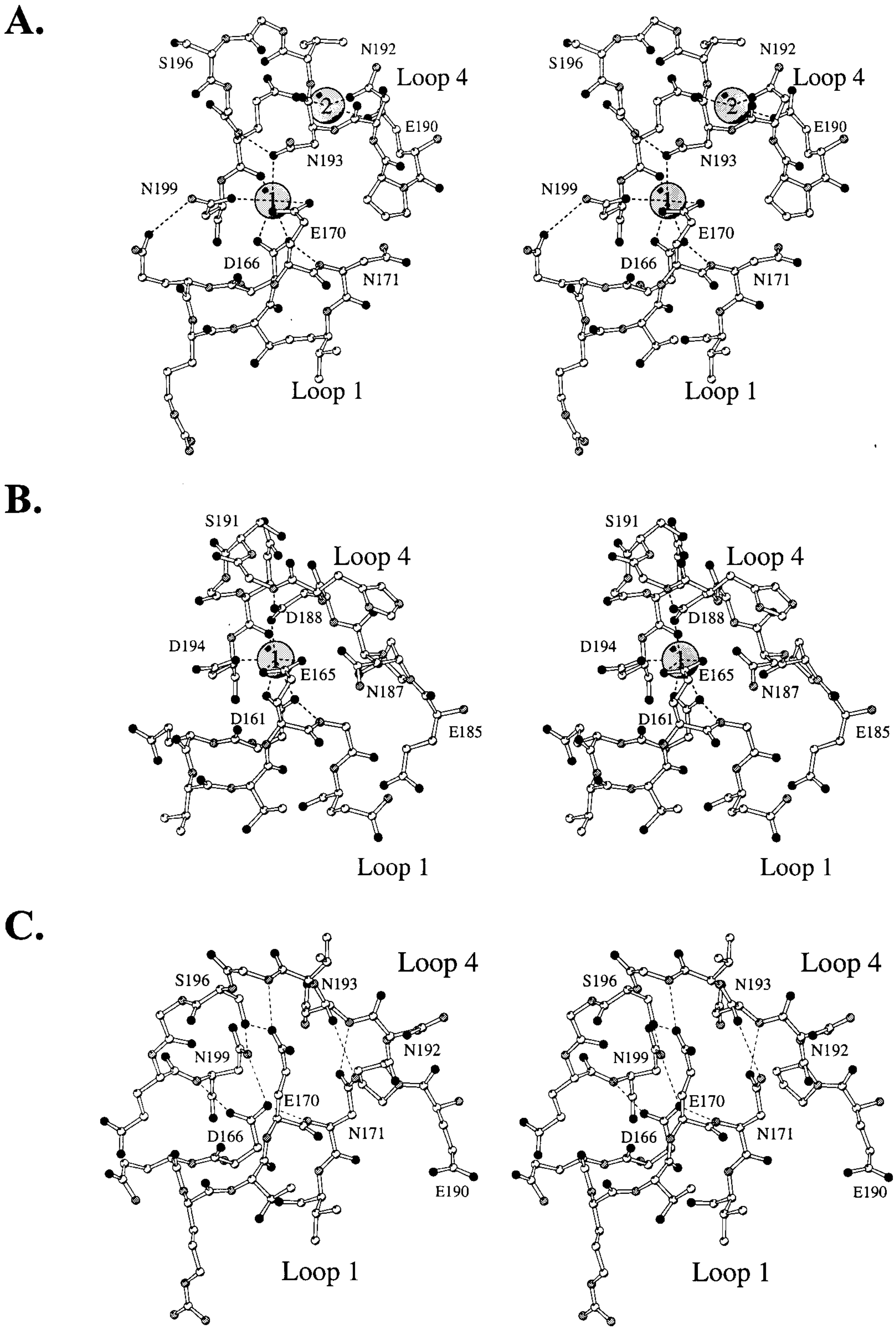

FIGURE 3: Stereoscopic views of interactions between loops 1 and 4. The main chain of loop 4 undergoes a rearrangement that is coupled to the cis–trans isomerization of the peptide bond preceding Pro^{191}: (A) two-ion MBP, (B) one-ion MBP, and (C) apo-MBP copy 1. All three structures have been superimposed as described in Figure 1, but the view taken is from the back-right-hand side of the structure as viewed in Figure 1. The Ca^{2+} coordination bonds formed in both two-ion MBP and one-ion MBP are replaced by an intricate pattern of hydrogen bonds in copy 1 of apo-MBP.

The conformation of the Pro^{191} peptide bond has large effects on the conformation of loop 4. Unlike loop 3, the structure of loop 4 is affected by the loss of Ca^{2+} from site 1, since it contributes two ligands to each Ca^{2+}-binding site (Figure 2A,B). In one-ion MBP (Figure 2E) and copy 1 of apo-MBP (Figure 2F), the conserved proline in site 2 is trans, and loop 4 extends farther from the protein than when the proline is in the cis conformation (Figure 2A–C). As noted earlier, the interactions at Ca^{2+} site 1 in two-ion MBP are preserved in one-ion MBP (Figure 3A,B). In copy 1 of apo-MBP, however, both loops 1 and 4 rearrange to compensate for the loss of both Ca^{2+}. Ca^{2+} ligands Asp^{166} and Glu^{170} in loop 1, and Asp^{199} in loop 4, as well as Ser^{196} and the adjacent protein backbone, rearrange to form an intricate hydrogen-

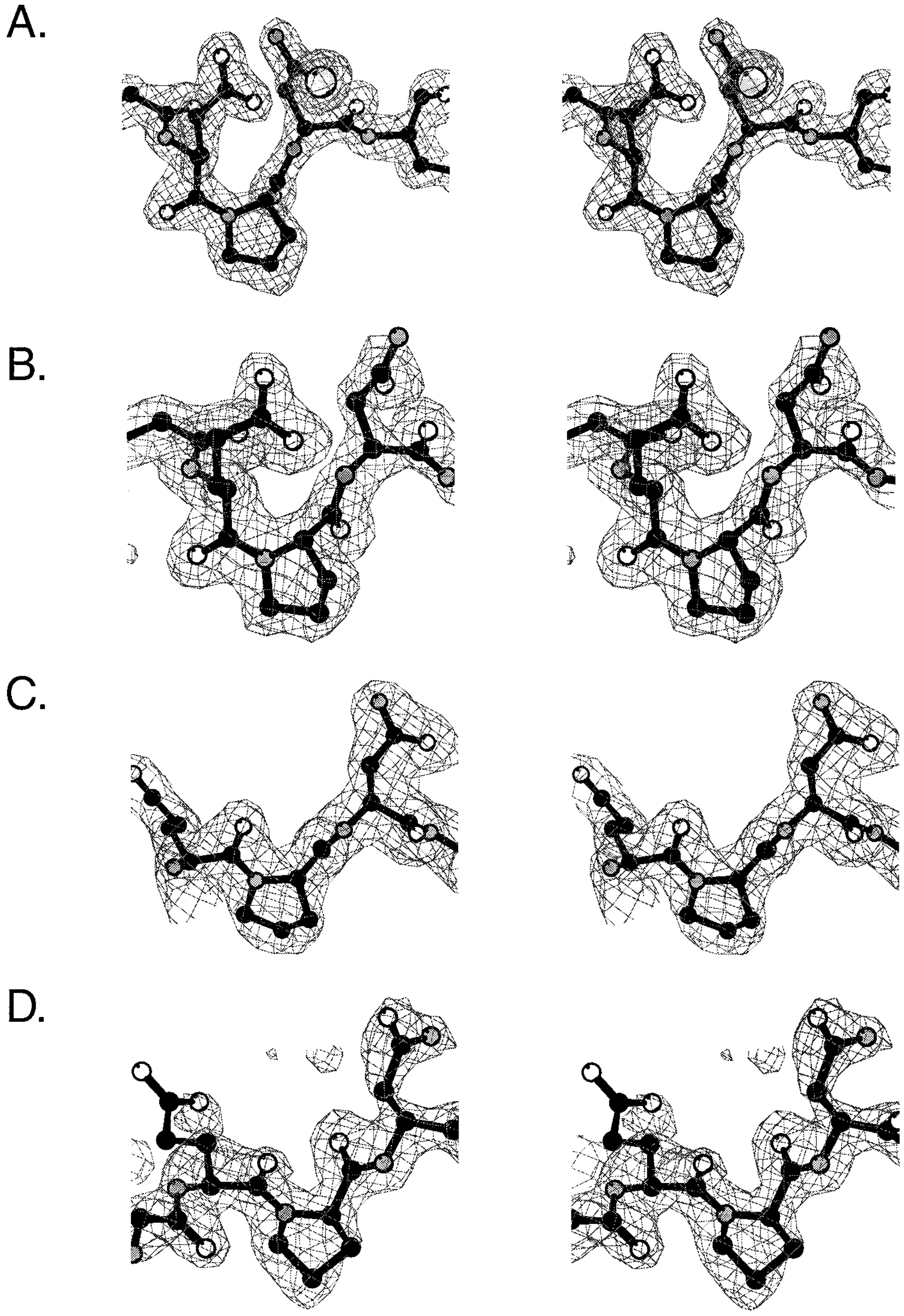

FIGURE 4: Stereoscopic views of the electron density around the conserved proline at Ca^{2+} site 2. Two-ion MBP (A) and apo-MBP copy 2 (B) adopt the cis conformation. One-ion MBP (C) and apo-MBP copy 1 (D) adopt the trans conformation. Residues 189−193 from MBP-C and residues 184−188 of MBP-A were omitted, and the structure was subjected to simulated annealing refinement starting at 1000 K, before the calculation of $|F_o| - |F_c|$ omit electron density maps. All maps are drawn at 2.4σ contour, except for Ca^{2+}-bound MBP-C, where the map is drawn at 3σ contour.

bond network (Figure 3C). As a consequence of the cis−trans isomerization of Pro^{191}, the side chain of the remaining Ca^{2+} site 1 ligand, Asn^{193}, is rotated by nearly 180° about the main chain. The backbone amide nitrogen and carbonyl oxygen atoms of Asn^{193} also participate in a new pair of hydrogen bonds with the side chain of Asn^{171}, which is a solvent-exposed residue at the tip of loop 1 in all of the Ca^{2+}-bound structures (Figure 3A). The formation of the new set of interactions seen in copy 1 of apo-MBP is facilitated by a slight rigid-body shift in the backbone of loop 1, side chain torsion angle rotations in Glu^{170} and Asn^{171}, and large rearrangements in the backbone and side chains of loop 4 (Figure 3C).

The loss of interactions between loop 4 and Ca^{2+} at sites 1 and 2 leads to a different set of interactions in the other copies of apo-MBP, where Pro^{191} adopts the cis conformation. In copy 2, loop 4 is well-defined by the electron density, but its conformation and the resulting interactions with loop 1 are very different from the well-ordered hydrogen-bond network seen in copy 1. In particular, Glu^{170} and Asn^{171}, which form important interactions between loop 4 and loop 1 in copy 1, are disordered in copy 2. Even though these

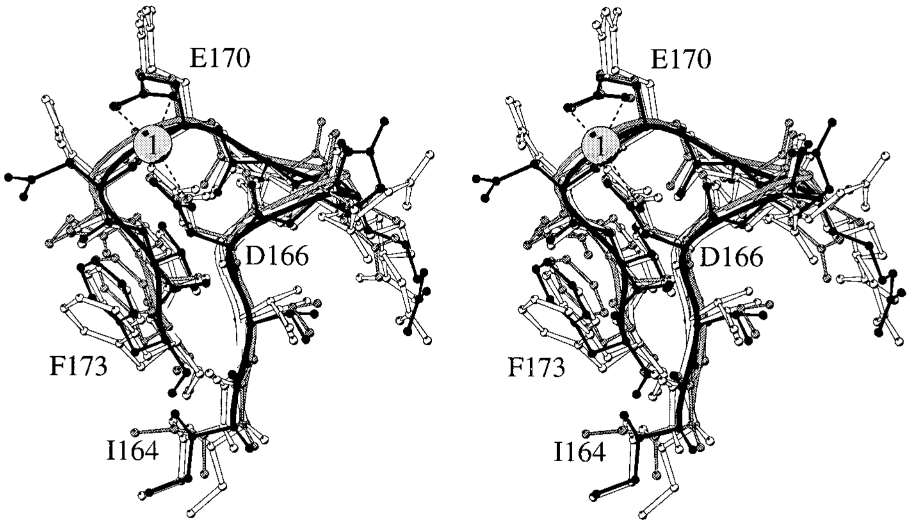

FIGURE 5: Stereoscopic views of loop 1. Residues 164−173 of apo-MBP copies 1 and 4 (white) and of two-ion MBP (black; Ca^{2+} drawn as a light gray sphere) are superimposed onto residues 159−168 of one-ion MBP (gray). The path of the α-carbon atoms is sketched with a smooth curve to aid in following the path of the loop. The main chain conformation is clearly conserved, as is the side chain conformation of a highly conserved bidentate ligand for Ca^{2+} 1 (Asp^{166} in MBP-C, Asp^{161} in MBP-A). The conformation of the side chain of the outer bidentate ligand in Ca^{2+} site 1 (Glu^{170} in MBP-C, Glu^{165} in MBP-A) extends away from the binding site in the absence of Ca^{2+}.

residues are not modeled, the visible portions of loops 1 and 4 indicate that Glu^{170} and Asn^{171} are too far away from loop 4 to make direct hydrogen-bond interactions. In copies 3 and 4, large segments of loop 4 are disordered, presumably because the loop is more flexible in the absence of the interactions normally mediated by Ca^{2+}.

DISCUSSION

The structures of one-ion MBP and apo-MBP indicate how Ca^{2+} stabilizes the structure of loops that are essential for carbohydrate-binding activity. The two Ca^{2+}-binding sites in the MBPs are roughly symmetrically disposed about loop 4 (Figure 2A). On one side of this loop, Ca^{2+} site 1 mediates interactions between loops 1 and 4; loss of Ca^{2+} at this site produces a rigid-body movement of loop 1 and more complex and extensive changes to loop 4. On the other side of loop 4, Ca^{2+} site 2 contains many interactions between loops 3 and 4, as well as interactions between both loops and the hydrophobic core. When Ca^{2+} site 2 is empty, the conformation of the peptide bond preceding the conserved proline residue at the junction of loops 3 and 4 determines whether the adjacent loops adopt a conformation similar to that found in the presence of Ca^{2+}. The retention of a cis-peptide bond at the junction of loops 3 and 4 locks the conformation of loop 3 and the proximal part of loop 4 into the Ca^{2+}-bound conformation even in the absence of Ca^{2+}. Isomerization of this bond to the trans conformation induces an extension of the loop away from the core of the protein, which involves the movement of Ca^{2+} ligand side chains by up to 12 Å. The dramatic rearrangements and increased flexibility in loops seen upon the removal of Ca^{2+}-dependent interactions explain the loss of carbohydrate binding, spectroscopic changes, and increased sensitivity to proteolysis that have been observed upon removal of Ca^{2+} from several C-type lectins (*4−10*).

The structures of apo-, one-ion, and two-ion forms of MBP show that the core of the CRD is unaffected by changes in the Ca^{2+}-binding loop regions. This observation suggests that the primary determinants of Ca^{2+}-binding affinities reside in the structure of the loops. However, a number of mutations in the hydrophobic core of the MBP-A CRD have secondary effects on Ca^{2+}-binding affinities (*27*). For example, the MBP-A mutant Ile^{147} → Thr, located in helix 2, binds Ca^{2+} with roughly 5-fold lower affinity than wild-type MBP-A. Preliminary analysis of the Ca^{2+}-saturated form of this mutant[3] does not show any significant changes in the structure of the CRD. Mutations in the hydrophobic core may affect Ca^{2+}-binding affinities by stabilizing conformations of the Ca^{2+}-binding loops that can only occur in the absence of Ca^{2+}, so structures of the apo forms of this and other mutants may be needed to determine how mutations in the hydrophobic core can affect Ca^{2+} binding. The apo-MBP structures described in this paper, however, do not suggest how Ca^{2+}-dependent structural changes in the loops are linked to structural changes in the CRD core.

An interesting parallel exists between the Ca^{2+}-induced peptide isomerization seen in the MBPs and a metal-ion-coupled peptide isomerization event in the legume lectins. An unusual nonprolyl cis-peptide is a conserved feature of the legume lectins (*42*). As in the MBPs, metal binding is crucial for the formation of a functional carbohydrate-binding site, and the cis conformation of this peptide bond is required for the proper positioning of at least one of the metal-binding residues. High-resolution structures of apo- and one-metal forms of concanavalin A show that the peptide bond preceding Asp^{208} adopts the trans conformation in the absence of metals (*43*, *44*). As in the case of the MBPs, the isomerization of this peptide bond is associated with large changes in the path taken by the adjacent segments of the metal-binding loop. Under physiological conditions, peptide-bond isomerization is a slow process because of the partial double-bond character of the peptide bond (*45, 46*). Very slow conformational changes associated with metal binding observed in concanavalin A, with half-lives of many hours,

---

[3] A. Gasch, A. Kolatkar, K. Ng, and W. Weis, unpublished observations.

have been attributed to the isomerization of the Asp^{208} peptide bond (*47*). Likewise, kinetic analysis of Ca^{2+} binding to MBP-C reveals a slow phase which suggests that the structural changes seen in one-ion MBP and apo-MBP crystals reflect conformational changes of the protein in solution (*48*).

It is interesting to consider whether the Ca^{2+}-dependent structural transitions observed for the MBPs may be exploited for specific biological functions. Many intracellular Ca^{2+}-binding proteins, such as, troponin C, calmodulin, and recoverin, couple the binding of Ca^{2+} to a major conformational change for the purpose of signaling a change in Ca^{2+} concentration to an intracellular effector (*49*). Intracellular Ca^{2+}-binding proteins are able to act as signaling molecules because the cell maintains a large Ca^{2+} concentration gradient across the cell membrane, thus allowing spatially and temporally transient bursts of Ca^{2+} to trigger a wide range of physiological effects (*50*). In contrast, extracellular proteins appear to be bathed in a relatively high and constant amount of Ca^{2+}, which limits the possibilities for generating large changes in Ca^{2+} concentration for the purposes of signaling or regulation. Nevertheless, Ca^{2+}-dependent structural transitions have been observed in several extracellular proteins involved in cell adhesion, including the selectins (*4*, *5*), cadherins (*51*), and integrins (*52*). These observations have led to the suggestion that transient changes in Ca^{2+} concentrations outside of the cell may also be exploited for regulatory purposes, although mechanisms for generating such changes in Ca^{2+} concentration are poorly understood (*53*, *54*).

An important role for a Ca^{2+}-dependent conformational changes in cell-surface C-type CRDs has been proposed for the process of receptor-mediated endocytosis (*7*, *55*, *56*). Several C-type lectins, including the mammalian asialoglycoprotein receptors, the macrophage galactose receptor, and the macrophage mannose receptor, are endocytic receptors. These proteins bind carbohydrate ligands at the cell surface under conditions of neutral pH and millimolar concentrations of Ca^{2+}. Following the binding of ligands, the membrane-bound receptor−ligand complex is endocytosed via a clathrin-coated vesicle. Once inside the cell, the vesicle is acidified, which triggers the release of Ca^{2+} from the lectin receptor and the dissociation of the ligand. The soluble contents of the vesicle are then directed toward the lysosome, while the membrane-bound receptors are returned to the cell surface. Once they return to the neutral pH environment of the cell surface, the lectin receptors regain the ability to bind Ca^{2+} and carbohydrate ligands, allowing them to participate in another round of endocytosis and ligand transport.

Although the MBPs are not known to participate in a cycle of reversible Ca^{2+} binding and release, it is likely that bona fide recycling endocytic receptors in the C-type lectin family share many of the structural features of the MBPs. Sequence comparisons (*57*), mutagenesis (*58*−*60*), and structural studies (*11*, *16*) suggest that the mammalian hepatic asialoglycoprotein receptors, the macrophage galactose receptor, and the macrophage mannose receptor all contain Ca^{2+} site 2. Moreover, a proline residue flanked by two conserved ligands for this binding site is universally conserved in the endocytic receptors, which suggests that the isomerization of the peptide bond preceding the conserved proline occurs in the endocytic receptors. Some structural features, such as the glycine-rich extension of loop 4 in the asialoglycoprotein receptors (*16*, *58*) and differences in the position of Ca^{2+} site 1 in the macrophage mannose receptor (*60*), will likely lead to differences in the details of Ca^{2+}-dependent conformational changes. Further studies will be needed to explore how Ca^{2+} binding is coupled to functionally important structural transitions in other C-type lectins.

ACKNOWLEDGMENT

We thank Dr. Kurt Drickamer for providing the ME-144 protein and for helpful comments on the manuscript. We also thank A. Kolatkar for advice and comments on the manuscript.

REFERENCES

1. Drickamer, K. (1993) *Curr. Opin. Struct. Biol. 3*, 393−400.
2. Weis, W. I., Drickamer, K., and Hendrickson, W. A. (1992) *Nature 360*, 127−134.
3. Ewart, K. V., Yang, D. S. C., Ananthanarayanan, V. S., Fletcher, G. L., and Hew, C. L. (1996) *J. Biol. Chem. 271*, 16627−16632.
4. Anostario, M., Jr., and Huang, K.-S. (1995) *J. Biol. Chem. 270*, 8138−8144.
5. Geng, J.-G., Moore, K. L., Johnson, A. E., and McEver, R. P. (1991) *J. Biol. Chem. 266*, 22313−22318.
6. Andersen, T. T., Freytag, J. W., and Hill, R. L. (1982) *J. Biol. Chem. 257*, 8036−8041.
7. Loeb, J. A., and Drickamer, K. (1988) *J. Biol. Chem. 263*, 9752−9760.
8. Haagsman, H. P., Sargeant, T., Hauschka, P. V., Benson, B. J., and Hawgood, S. (1990) *Biochemistry 29*, 8894−8900.
9. Weis, W. I., Crichlow, G. V., Murthy, H. M. K., Hendrickson, W. A., and Drickamer, K. (1991) *J. Biol. Chem. 266*, 20678−20686.
10. Mullin, N. P., Hall, K. T., and Taylor, M. E. (1994) *J. Biol. Chem. 269*, 28405−28413.
11. Weis, W. I., Kahn, R., Fourme, R., Drickamer, K., and Hendrickson, W. A. (1991) *Science 254*, 1608−1615.
12. Ng, K. K.-S., Drickamer, K., and Weis, W. I. (1996) *J. Biol. Chem. 271*, 663−674.
13. Sheriff, S., Chang, C. Y., and Ezekowitz, R. A. B. (1994) *Nat. Struct. Biol. 1*, 789−794.
14. Graves, B. J., Crowther, R. L., Chandran, C., Rumberger, J. M., Li, S., Huang, K.-S., Presky, D. H., Familletti, P. C., Wolitzky, B. A., and Burns, D. K. (1994) *Nature 367*, 532−538.
15. Nielsen, B. B., Kastrup, J. S., Rasmussen, H., Holtet, T. L., Graversen, J. H., Etzerodt, M., Thogersen, H. C., and Larsen, I. K. (1997) *FEBS Lett. 412*, 388−396.
16. Kolatkar, A. R., and Weis, W. I. (1996) *J. Biol. Chem. 271*, 6679−6685.
17. Ng, K. K.-S., and Weis, W. I. (1997) *Biochemistry 36*, 979−988.
18. Ashwell, G., and Harford, J. (1982) *Annu. Rev. Biochem. 51*, 531−554.
19. Drickamer, K., Dordal, M. S., and Reynolds, L. (1986) *J. Biol. Chem. 261*, 6878−6886.
20. Quesenberry, M. S., and Drickamer, K. (1991) *Glycobiology 1*, 615−621.
21. Lee, R. T., Ichikawa, Y., Fay, M., Drickamer, K., Shao, M.-C., and Lee, Y. C. (1991) *J. Biol. Chem. 266*, 4810−4815.
22. Iobst, S. T., Wormald, M. R., Weis, W. I., Dwek, R. A., and Drickamer, K. (1994) *J. Biol. Chem. 269*, 15505−15511.
23. Quesenberry, M. S., Lee, R. T., and Lee, Y. C. (1997) *Biochemistry 36*, 2724−2732.
24. Lee, R. T., and Lee, Y. C. (1997) *Glycoconjugate J. 14*, 357−363.
25. Weis, W. I., and Drickamer, K. (1994) *Structure 2*, 1227−1240.
26. Burling, F. T., Weis, W. I., Flaherty, K. M., and Brünger, A. T. (1996) *Science 271*, 72−77.

27. Quesenberry, M. S., and Drickamer, K. (1992) *J. Biol. Chem. 267*, 10831−10841.
28. Sastry, K., Zahedi, K., Lelias, J.-M., Whitehead, A. S., and Ezekowitz, R. A. B. (1991) *J. Immunol. 147*, 692−697.
29. Mogues, T., Ota, T., Tauber, A. I., and Sastry, K. N. (1996) *Glycobiology 6*, 543−550.
30. Hoppe, H.-J., Barlow, P. N., and Reid, K. B. M. (1994) *Protein Sci. 3*, 1143−1158.
31. Otwinowski, Z. (1993) in *Data Collection and Processing* (Sawyer, L., Isaacs, N., and Bailey, S., Eds.) pp 56−62, SERC Daresbury Laboratory, Daresbury, U.K.
32. Brünger, A. T. (1992) *X-PLOR manual, version 3.1*, Yale University, New Haven, CT.
33. Brünger, A. T. (1990) *Acta Crystallogr., Sect. A 46*, 46−57.
34. Brünger, A. T., Adams, P. D., Clore, G. M., Gros, P., Grosse−Kunstleve, R. W., Jiang, J.-S., Kuszewski, J., Nilges, M., Pannu, N. S., Read, R. J., Rice, L. M., Simonson, T., and Warren, G. L. (1998) *Acta Crystallogr., Sect. D 54*, 905−921.
35. Pannu, N. S., and Read, R. J. (1996) *Acta Crystallogr., Sect. A 52*, 659−668.
36. Jiang, J. S., and Brünger, A. T. (1994) *J. Mol. Biol. 243*, 100−115.
37. Collaborative Computational Project No. 4. (1994) *Acta Crystallogr., Sect. D 50*, 760−763.
38. Hodel, A., Kim, S.-H., and Brünger, A. T. (1992) *Acta Crystallogr., Sect. A 48*, 851−858.
39. Jones, T. A., Zou, J.-Y., Cowan, S. W., and Kjeldgaard, M. (1991) *Acta Crystallogr., Sect. A 47*, 110−119.
40. Sheriff, S., and Hendrickson, W. A. (1987) *Acta Crystallogr., Sect. A 43*, 118−121.
41. Luzzati, V. (1952) *Acta Crystallogr. 5*, 802−810.
42. Rini, J. M. (1995) *Annu. Rev. Biophys. Biomol. Struct. 24*, 551−577.
43. Bouckaert, J., Loris, R., Poortmans, F., and Wyns, L. (1995) *Proteins 23*, 510−524.
44. Bouckaert, J., Poortmans, F., Wyns, L., and Loris, R. (1996) *J. Biol. Chem. 271*, 16144−16150.
45. Brandts, J. F., Halvorson, H. R., and Brennan, M. (1975) *Biochemistry 14*, 4953−4963.
46. Stein, R. L. (1993) *Adv. Protein Chem. 44*, 1−24.
47. Brewer, C. F., Brown, R. D., and Koenig, S. H. (1983) *J. Biomol. Struct. Dyn. 1*, 961−997.
48. Ng, K. K.-S., and Weis, W. I. (1998) *Biochemistry 37*, 17977−17989.
49. Ikura, M. (1996) *Trends Biochem. Sci. 21*, 14−17.
50. Berridge, M. J. (1997) *J. Physiol. (London) 499*, 291−306.
51. Pokutta, S., Herrenknecht, K., Kemler, R., and Engel, J. (1994) *Eur. J. Biochem. 223*, 1019−1026.
52. Philips, D. R., Charo, I. F., and Scarborough, R. M. (1991) *Cell 65*, 359−362.
53. Hebert, S. C., and Brown, E. M. (1995) *Curr. Opin. Struct. Biol. 7*, 484−492.
54. Maurer, P., Hohenester, E., and Engel, J. (1996) *Curr. Opin. Struct. Biol. 8*, 609−617.
55. DiPaola, M., and Maxfield, F. R. (1984) *J. Biol. Chem. 259*, 9163−9171.
56. Schwartz, A. L. (1995) *Pediatr. Res. 38*, 835−843.
57. Drickamer, K. (1992) *Nature 360*, 183−186.
58. Iobst, S. T., and Drickamer, K. (1994) *J. Biol. Chem. 269*, 15512−15519.
59. Iobst, S. T., and Drickamer, K. (1996) *J. Biol. Chem. 271*, 6686−6693.
60. Mullin, N. P., Hitchen, P. G., and Taylor, M. E. (1997) *J. Biol. Chem. 272*, 5668−5681.
61. Brünger, A. T. (1992) *Nature 355*, 472−475.
62. Laskowski, R. A., MacArthur, M. W., Moss, D. S., and Thornton, J. M. (1993) *J. Appl. Crystallogr. 26*, 283−291.
63. Kleywegt, G. J., and Jones, T. A. (1996) *Acta Crystallogr., Sect. D 52*, 842−857.
64. Esnouf, R. M. (1997) *J. Mol. Graphics Model. 15*, 132−134.
65. Kraulis, P. J. (1991) *J. Appl. Crystallogr. 24*, 946−950.

BI981972A